applied sciences

MDPI

Article

Influence of Impurity Scattering on Surface Plasmons in Graphene in the Lindhard Approximation

Mousa Bahrami [1,*] and Panagiotis Vasilopoulos [2]

[1] Bita Quantum AI, 2021 Av. Atwater, Montréal, QC H3H 2P2, Canada
[2] Department of Physics, Concordia University, 7141 Sherbrooke Ouest, Montréal, QC H4B 1R6, Canada; p.vasilopoulos@concordia.ca
* Correspondence: m_bahra@live.concordia.ca

Abstract: We study the influence of impurity scattering on transverse magnetic (TM) and transverse electric (TE) surface plasmons (SPs) in graphene using the Lindhard approximation. We show how the behaviour and domains of TM SPs are affected by the impurity strength γ and determine the critical value γ_c below which no SPs exist. The quality factor of TM SPs, for single-band and two-band transitions, is proportional to the square of $\alpha\lambda_{SP}/\gamma$, with α being the fine-structure constant and λ_{SP} being the plasmon wavelength. In addition, we show that impurity scattering suppresses TE SPs.

Keywords: surface plasmons; scattering; quantum well; wire and dot devices; optical properties

Citation: Bahrami, M.; Vasilopoulos, P. Influence of Impurity Scattering on Surface Plasmons in Graphene in the Lindhard Approximation. *Appl. Sci.* **2021**, *11*, 10147. https://doi.org/10.3390/app112110147

Academic Editors: Petr Korusenko and Sergey Nesov

Received: 8 October 2021
Accepted: 26 October 2021
Published: 29 October 2021

1. Introduction

The building blocks of all contemporary digital electronic devices, communications, and circuits, which are employed to process, transport, and store information, are made up of metal-oxide-semiconductor field-effect transistors (MOSFETs) [1–3]. As many issues in the vast majority of scientific fields and economy rely on very fast transistors nowadays, the demand for low-cost and high-speed MOSFETs with lower power consumptions is very strong. The clock speed of information processing in transistors directly pertains to the size, miniaturization, and density of comprised elements in them [4]. In contrast, smaller transistors have high speeds but there is a strong challenge related to the interconnect number. By reducing the size of the latter, the delay time increases and imposes critical limitations on the clock speed frequencies [3] . Fiber-optic cables are another promising candidate for communication and the transportation of information due to their high transparency [2,5]. They are capable of carrying information about one thousand times faster compared to electronic circuits. In addition, in fiber-optic cables, light packets carry information as they travel over long distances [3].

These fiber-optic features suggest a synergy between these two technologies [6]. However, because the strength of light–matter interactions in these dielectric materials is not sufficient to exhibit nonlinear behaviour, they require a high power density and volume and lead to limitations in their integration with electronic circuits [7]. The major obstacle is a consequence of the diffraction limit, which does not allow light to squeeze in a region smaller than its wavelength [2,3,8]. One promising candidate to face this challenge is surface plasmons (SPs) [9–13]. An SP is a sub-wavelength evanescent electromagnetic wave that propagates at the interface of a metallic-dielectric medium [14,15]. The SP frequency in the noble metal is in the order of femtoseconds, reflecting higher clock speeds compared with state-of-the-art transistors [1]. SPs enable us to investigate the light–matter interaction in the sub-wavelength area, which is otherwise inaccessible. SPs allow one to manipulate and route light at the nanoscale [3,6,12,13,16]. They have a plethora of prospective applications such as optical switches, spacers, near-field optical microscopy, bio-sensing and nanosensors, improving efficiency of light-emitting diodes (LEDs), solar cells, cancer treatment, biomedical tests, quantum sensing, and teleportation [17–26].

One of the most interesting materials that supports SPs at room temperature is graphene. In contrast to bulk-dielectric systems that support only transverse magnetic (TM) SPs [27], graphene also supports transverse electric (TE) and TM SPs [28]. In addition, SP losses in graphene are lower than those in noble metals. Scattering, e.g., by impurities, can profoundly affect SPs. In the literature, these effects has been regarded phenomenologically by heuristically introducing a Drude-form conductivity in the long-wavelength limit [29,30]. In this paper, we borrow some results from Ref. [31] and evaluate TM and TE SPs in graphene in the presence of impurity scattering.

In Section 2, we present some general expressions for the Lindhard polarization in the presence and absence of impurities as well as the transmission and reflection amplitudes. In Section 3, we investigate TM SPs in graphene for intra-band and inter-band transitions, renamed, for clarity and brevity, as SB and TB transitions, in the presence and absence of impurity scattering. In Section 4, we evaluate the quality factor (QF) of these SPs. In Section 5, we evaluate transverse electric surface plasmons for SB and TB transitions. Our summary follows in Section 6.

2. Scattering-Dependent Optical Properties

We consider a graphene sheet in between two media with the permittivities ϵ_1 and ϵ_2, respectively. The corresponding reflection and transmission coefficients are obtained by satisfying the boundary conditions for the longitudinal and perpendicular components of the TM field. The transmission coefficient is given by [15]

$$t(q,\omega) = 2\left[\frac{n_2}{n_1} + \frac{\cos\theta_t}{\cos\theta_i} + \frac{\sigma(q,\omega)\cos\theta_t}{n_1\epsilon_0 c}\right]^{-1}. \tag{1}$$

Here, $\epsilon_0 n_i^2 = \epsilon_i$, $i = 1, 2$, n_i is the refractive index, σ is the conductivity of graphene, and θ_i, θ_t are the angles of incidence and transmission, respectively. In general, the index n depends on the momentum and frequency, but here we assume that it is constant. The conductivity can be evaluated as, e.g., in [15]. The result is

$$\sigma(q,\omega) = ie^2\omega\chi(q,\omega)/q^2, \tag{2}$$

where χ is the polarization function also known as density–density response function. The polarization function can be evaluated in the absence or presence of the Coulomb interaction. Here, we employ the Lindhard approximation, in which the effects of electron–electron interactions and the local field factor are neglected. It is worth pointing out that including many-body effects such as electron–electron interaction or exchange effects, known as the random-phase approximation (RPA) or Hubbard approximation, respectively, provide a good insight about the system response but its evaluation becomes very complicated. For the sake of simplicity, we limit our calculation to the Lindhard approximation in which the computation time is much shorter than in the RPA or Hubbard approximation. The Lindhard polarization function in the presence of impurity scattering, within the van Hove limit, is given by [31]

$$\chi^0(q,\omega) = \chi^0_{non}(q,\omega) + \chi^0_{imp}(q,\omega), \tag{3}$$

where χ^0_{non} and χ^0_{imp} are the polarization functions in the absence [32] and presence [31] of impurity scattering, respectively. Since we are interested in SPs with lower and higher energies than the Fermi energy, which are known as intra- and inter-band SPs or SB and TB SPs, the polarization functions at zero temperature and in the long-wavelength limit [31,32] are given by

$$\chi'^{0,SB}_{non}(q',\omega') = \frac{q'^2}{\omega'^2},\ \chi'^{0,SB}_{imp}(q',\omega') = C(\omega',\gamma')/2, \tag{4}$$

$$\chi'^{0,TB}_{non}(q',\omega') = \frac{M(\omega')q'^2}{2\omega'},\ \chi'^{0,TB}_{imp}(q',\omega') = C(\omega',\gamma'), \tag{5}$$

where we introduced the dimensionless parameters χ'^0, q', ω', and γ' ($\chi'^0 = \chi^0 \chi \hbar v_F/k_F$, $q' = q/k_F$, $\omega' = \hbar\omega/E_F$, $\gamma' = \hbar\gamma/E_F$ to simplify all expressions. E_F, $k_F = E_F/\hbar v_F$, and v_F are the Fermi energy, wave vector, and velocity, respectively. We used $v_F = 9 \times 10^5$ m/s. Further,

$$C(\omega', \gamma') = \frac{1 - \delta_{\gamma',0}}{\omega' + i\gamma'}, \; M(\omega') = \left[A(\omega') - i\frac{\pi}{2}\Theta(\omega' - 2)\right], \tag{6}$$

and

$$A(\omega') = \frac{2}{\omega'} + \frac{1}{2}\ln\left|\frac{2 - \omega'}{2 + \omega'}\right|. \tag{7}$$

The form of the response function (3) is derived in Ref. [33] for *homogeneous systems:* χ_{non} is independent of the scattering, while χ_{im} depends on it but it was not explicitly evaluated in Refs. [33,34]. Importantly, when the response is evaluated from the collisionless Boltzmann equation, one obtains *the term* $\chi^{0,SB}_{non}$ [35] and the term $\chi^{0,TB}_{non}$ is absent. The latter term is obtained, e.g., in Refs. [28,32] using Kubo formulas.

In Figure 1, we plot the real and imaginary parts of the TB polarization function in the absence of impurities. The real part shows that its magnitude decreases, with increasing frequency, for all values of the momentum. The decrease is very fast for large frequencies. In contrast, the imaginary part decreases dramatically, when the momentum decreases, for $\omega' > 2$ and vanishes for $\omega' \leqslant 2$. The divergent behaviour of the real part of the polarization function in the absence of impurities, $Re\chi_{non}$, due to the logarithmic term in Equation (7) at $\omega' = 2$ is easily noticeable in the contour plot. In addition, the contour plot of the imaginary part of $Re\chi_{non}$ shows its step-function behaviour for $\omega' \leq 2$ in Equation (6), where it vanishes.

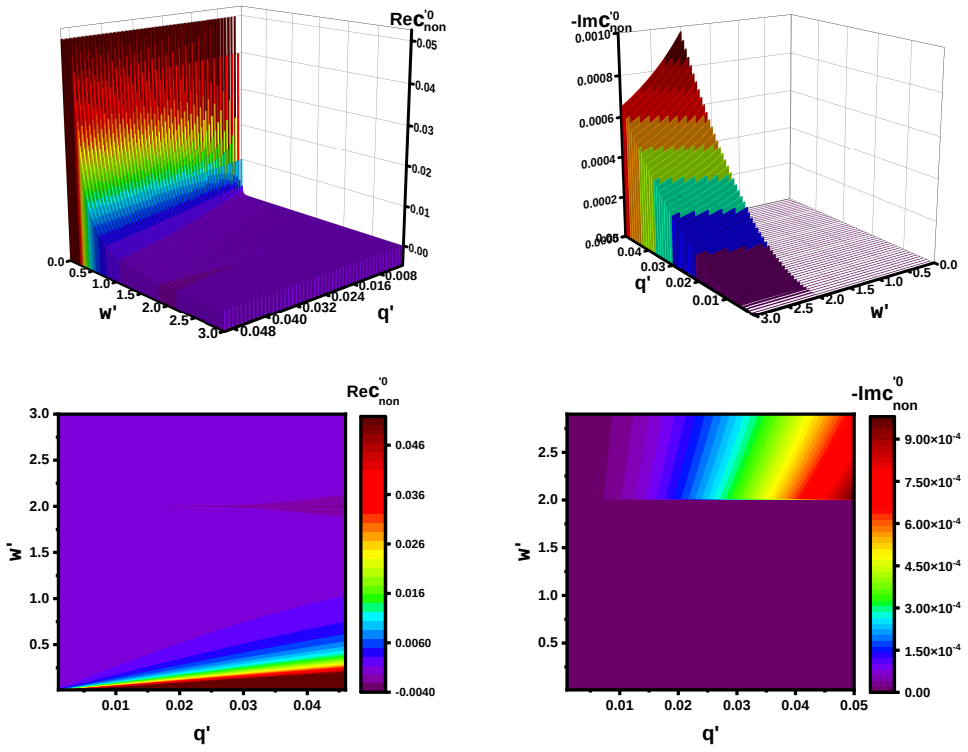

Figure 1. 3D bar and contour plot of the real and imaginary parts of the polarization function $\chi'^{0,TB}_{non}$ in the absence of impurities.

The real and imaginary parts of $\chi'^{0,TB}_{imp}$, when impurity scattering is present, are shown in Figure 2. In contrast with $\chi'^{0,TB}_{non}$, $\chi'^{0,TB}_{imp}$ does not rely on momentum since γ' has been assumed to be independent of it. Therefore, it is shown in terms of the impurity strength and frequency. It is worth pointing out that the order of magnitude of $\chi'^{0,TB}_{imp}$ is much larger

than $\chi_{non}^{'0,TB}$. Consequently, we expect that $\chi_{imp}^{'0,TB}$ will be higher than $\chi_{non}^{'0,TB}$. As seen in the contour plots of the real and imaginary parts of χ_{im}, their values at low frequencies and low impurity concentrations are approximately three orders of magnitude higher than the other parts of their spectrum.

In Figure 3, we plot the real and imaginary parts of χ for a typical impurity strength, $\gamma' = 0.06$. As clearly shown in the contour plots, for low frequencies, $\omega' \leq 0.05$, the real part of χ increases dramatically with increasing momentum. However, for a typical momentum and $\omega' \geq 0.1$, it decreases. On the other hand, its imaginary part increases with frequency for a typical momentum, reflecting the fact that for larger frequencies the energy dissipation increases.

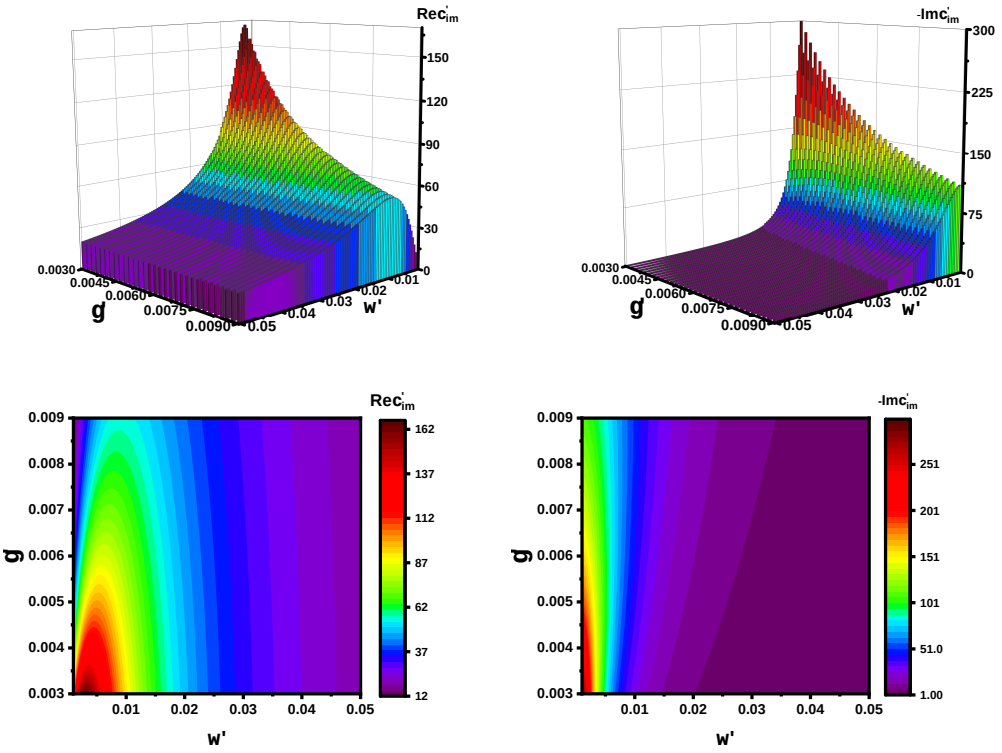

Figure 2. 3D bar and contour plot of the real and imaginary parts of polarization function in the presence of impurity, $\chi_{imp}^{'0,TB}$.

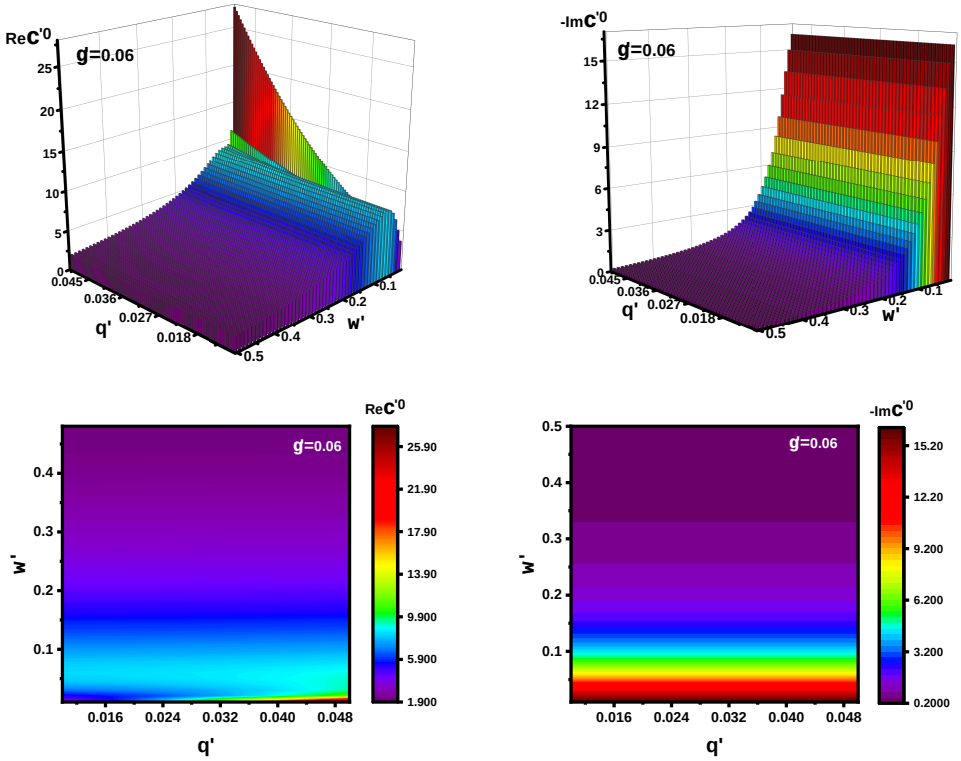

Figure 3. 3D bar and contour plot of the real and imaginary parts of χ for $\gamma' = 0.06$.

3. Transverse Magnetic Surface Plasmons

The poles of the transmission or reflection coefficients give the SPs [15,36]. For TM modes, we have

$$q = i\omega\epsilon_0(n_1^2 + n_2^2)/\sigma(q,\omega). \tag{8}$$

We emphasize that Equation (3) is valid only for SP momenta that are much larger than that of light, $q \gg \omega/c$. Since the polarization function can be evaluated in the Lindhard, random-phase or Hubbard approximation, so can the SPs resulting from (8) due to the relation between χ and conductivity, Equation (2). The simplest approximation on which we focus here is the Lindhard one that neglects the effects of the Coulomb interaction and local field factor [31]. Since the polarization function acquires different values for SB and TB transitions, the SPs would be different in each case. Notice that the real part of the transmission pole yields an SP mode [36], while its imaginary part is responsible for dissipation. For SB transitions, Equations (2), (4), and (8) give

$$q'^2 - q'\beta\omega'^2 + \frac{\omega'^2}{2}\mathfrak{Re}C(\omega',\gamma') = 0 \tag{9}$$

with $\beta = v_F(n_1^2 + n_2^2)/4\alpha c$ and α, v_F, and c being the fine-structure constant, Fermi velocity, and light velocity, respectively. The physical solution is given by

$$q' = \frac{1}{2}\left[\beta\omega'^2 + \left[(\beta\omega'^2)^2 - 2\omega'^2\mathfrak{Re}C(\omega',\gamma')\right]^{1/2}\right]. \tag{10}$$

For TB transitions using Equations (2), (5) and (8) we obtain the physically acceptable solution

$$q' = \frac{\omega'\beta}{A(\omega')}\left(1 + \left[1 - \frac{2A(\omega')}{\omega'\beta^2}\mathfrak{Re}C(\omega',\gamma')\right]^{1/2}\right). \tag{11}$$

Notice that there are other solutions for Equations (10) and (11) with the $+$ sign in front of the square root $+[..]^{1/2}$ replaced by a $-$ sign. However, these solutions are unphysical and therefore rejected.

In Figures 4a and 5a, we show the TM SP dispersion relation, for several values of γ', obtained with $n_1 = 1$ and $n_2 = 2$. To render its behaviour more clear, we replotted it in Figures 4b and 5b for a smaller range of q'. As seen, with decreasing γ' the acceptable value of q' increases and that for SB transitions is smaller than for the TB ones. Moreover, the SP frequency is larger in the TB case for typical values of q'. In either case, the group velocity $\partial\omega/\partial q$ is nearly constant and independent of the impurity strength. The SP dispersion changes when the strength γ' is varied. This can be understood as follows. A coherent ensemble of dipole moments (DMs) oscillating about their equilibrium configuration, under a phase matching condition, starts to generate an evanescent electromagnetic field that propagates at the interface of the metallic-dielectric medium. Damping effects due to defects, impurities, or electron–phonon interactions are expected to reduce the effective number of these coherent DMs. That is, a higher value of γ' leads to a higher scattering probability and reduces the number of coherent DMs. Hence, the energy of an EMF that originated from an ensemble of DMs for a lower γ', with the same momentum, is larger than that for a higher γ'.

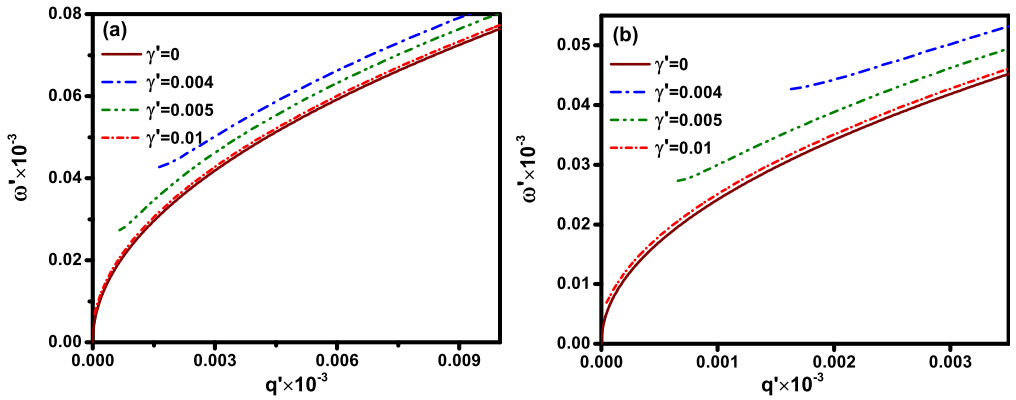

Figure 4. (**a**) SB TM SP for different values of γ'. (**b**) The segment of (a) for $q' \times 10^{-3} \leq 0.0035$.

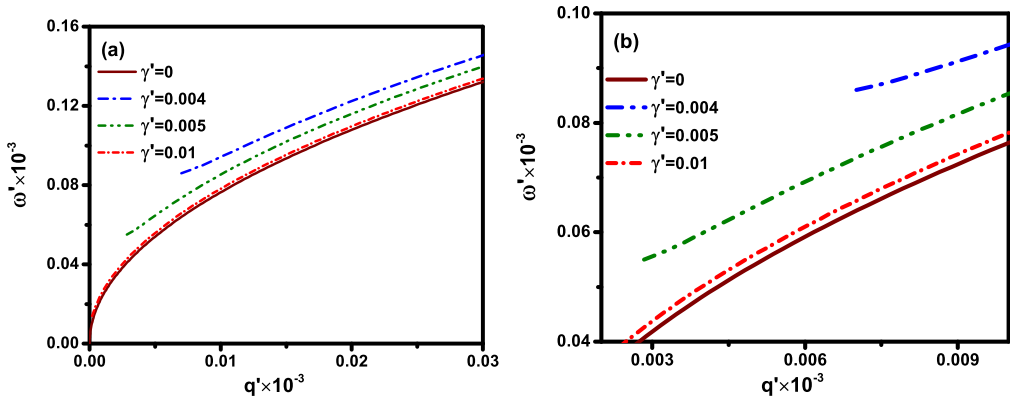

Figure 5. (**a**) TB TM SP for different values of γ'. (**b**) The segment of (a) for $q' \times 10^{-3} \leq 0.01$.

In Figures 6 and 7, we plot the 3D TM SP spectrum and the (ω', γ') contour plot of SB and TB, respectively. As can be seen, for a fixed γ', increasing the SP frequency leads to momentum increases as well. The bars in these figures indicate the allowed values in a region where SPs exist. It can be seen, in particular in Figures 4 and 5, that below a critical value of γ', called γ'_c, no SPs exist. This critical strength γ'_c can be determined by setting the quantities $[..]^{1/2}$ to zero in Equations (10) and (11). This gives

$$\gamma_c'^{SB} = [2/\beta^2\omega' - \omega'^2]^{1/2}, \tag{12}$$

$$\gamma_c'^{TB} = \left[2A(\omega')/\beta^2 - \omega'^2\right]^{1/2}. \tag{13}$$

The strength γ_c' versus the SP frequency ω' is shown in Figure 8 for the SB and TB cases. In either case, γ_c' decreases very fast with an increase in the SP frequency. Moreover, for a fixed frequency, γ_c' is smaller in the SB case.

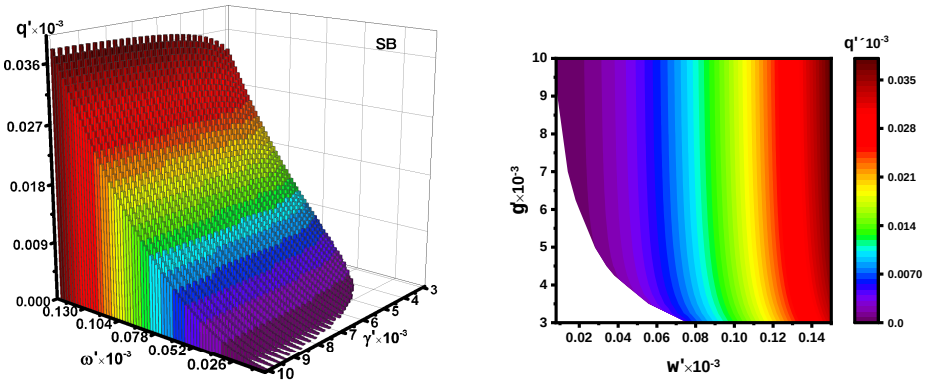

Figure 6. 3D bar and (γ', ω') contour plots of TM SB SPs.

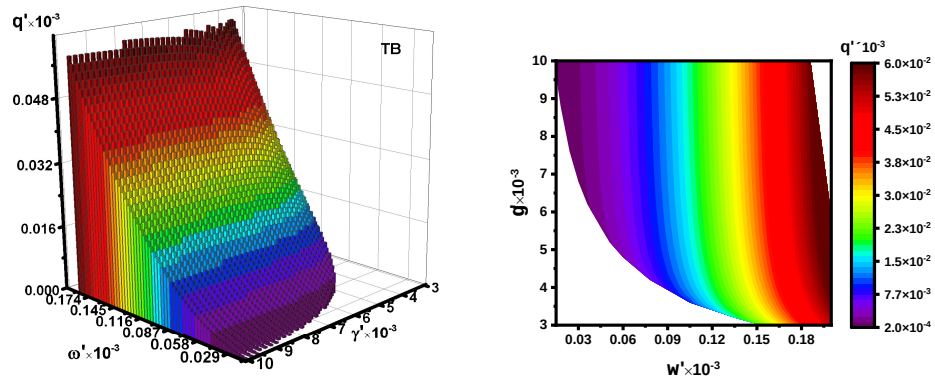

Figure 7. 3D bar and (γ', ω') contour plots of TM TB SPs.

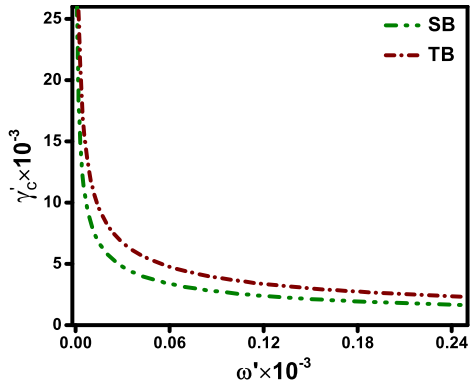

Figure 8. Spectrum of critical impurity versus SB and TB SP frequency.

4. Quality Factor

To efficiently transport high-speed information and energy, devices must, to the highest extent possible, have the least number of obstacles or defects, e.g., impurities, so that the energy dissipation is the lowest. Devices with the best functionality are usually distinguished by the quality factor (QF) defined as the ratio of the stored to the dissipated energy. The higher the QF, the higher the device functionality and performance are [37]. The QF is defined by

$$Q = \frac{U_{stor}}{U_{dis}} = \frac{U_0 - U_{dis}}{U_{dis}} = \frac{U_0}{U_{dis}} - 1, \tag{14}$$

where U_{stor}, U_{dis} and U_0 refer, respectively, to the stored, dissipated, and total energy densities. U_0 is the energy density of the incoming field, $U_0 = \epsilon_0 |E_I|^2/2$. The dissipated energy of the SP, U_{dis}, is

$$U_{dis} = \frac{1}{2}\epsilon_0 |E_{dis}|^2 = \frac{1}{2}\epsilon_0 |E_I|^2 \left| \Im\mathfrak{m}\, t(q'_{sp}, \omega'_{sp}) \right|^2, \tag{15}$$

where $\Im\mathfrak{m}\, t(q'_{sp}, \omega'_{sp})$ is the imaginary part of the transmission amplitude at the plasmon momentum and frequency. For SB and TB transitions, the results are

$$Q_{SB} = \left[\eta\, \Im\mathfrak{m}\, C(\omega'_{sp}, \gamma')/2q'_{sp} \right]^2 - 1, \tag{16}$$

$$Q_{TB} = \left[\eta D(\omega'_{sp}, \gamma')/2q'_{sp} \right]^2 - 1, \tag{17}$$

with

$$D(\omega'_{sp}, \gamma') = \Im\mathfrak{m}\, C(\omega'_{sp}, \gamma') + (\pi q'^2_{sp}/4\omega')\, \Theta(\omega' - 2), \tag{18}$$

and $\eta = 4\alpha c/(v_F n_1 n_2)$. For low frequencies, by combining Equations (10) and (16) in the SB case, or Equations (11) and (17) in the TB case, we obtain

$$Q \approx \alpha^2 \lambda^2_{sp}/\gamma'^2; \tag{19}$$

this result depends only on the fine-structure constant, the SP wavelength, and the impurity strength.

In Figure 9a,b, we show, respectively, the SB and TB QF of TM SPs versus their frequencies ω for several values of γ'. As seen, the QF decreases strongly with increasing frequency. In addition, for a fixed ω, the QF decreases, in both cases, upon increasing γ', which is expected since higher values of γ' imply an increase in dissipation. According to Equations (10) and (11), for low frequencies ω, the SP wavelength is proportional to ω^{-2}, see also Figure 9, and in both cases the QF decreases as ω^{-4}. As the dissipation is stronger in the TB case than in the SB one, cf. Equations (4) and (5), we expect that the QF will be higher in the SB case; indeed, this is made clear in Figure 9. Correspondingly, the energy density stored in the SB case is higher than in the TB one.

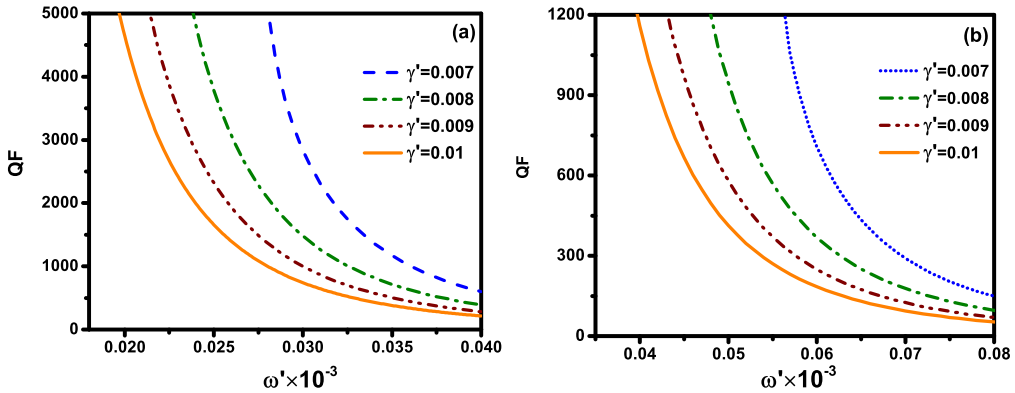

Figure 9. (**a**) SB and (**b**) TB TM SPs QF versus SP energy for several values of γ'.

5. Transverse Electric Surface Plasmons

As in the case of TM SPs, the transmission coefficient for TE SPs is given by [15]

$$t(k, \omega) = 2\left[1 + \frac{n_2 \cos\theta_t}{n_1 \cos\theta_i} + \frac{\sigma(k, \omega)}{n_1 \epsilon_0 c \cos\theta_i} \right]^{-1}. \tag{20}$$

Corresponding to Equation (8), we find

$$k = i\sigma(k,\omega)\omega/2\epsilon_0 c^2. \tag{21}$$

In the SB case there are no TE SPs as in the absence of scattering [28]. In the TB **case** corresponding to Equation (9), we obtain

$$q'^3 + aq'^2 + b = 0, \tag{22}$$

where $a = 2\alpha c\omega' A(\omega')/v_F$ and $b = 4\alpha c\omega'^2 \Re\mathfrak{e}\, C(\omega',\gamma')/v_F$. Equation (22) has a real solution with negative value for q' which is unphysical. Accordingly, we infer that impurity scattering suppresses TE SPs in graphene.

6. Summary

We evaluated TM SPs in graphene for SB and TB transitions in the Lindhard approximation for the polarization function, in which the Coulomb interaction and local field factors are neglected, but thoroughly took into account scattering by impurities, see Equations (3)–(5), without making the usual, phenomenological change $\omega \to \omega + i\tau$ in the scattering-independent polarization function χ_{non}. The main results are as follows.

(1) Impurity scattering changes the spectrum of the TM surface plasmons. (2) The scattering strength γ restricts the SP domains for SB and TB transitions. Importantly, for each frequency, there is a critical scattering strength γ_c below which SPs do not exist. The strength γ_c decreases with frequency; it is very fast for very low frequencies and much less so for higher frequencies. (3) The quality factor (QF) is affected by the scattering. We found it approximately equal to the square of $\alpha\lambda_{SP}/\gamma$, where α is the fine-structure constant and λ_{SP} the wavelength; see Equation (19). For a fixed frequency, the QF decreases with γ for SB and TB transitions and is higher for the SB ones, cf. Figure 9. (4) TE SPs are suppressed by impurity scattering.

We hope these findings will be tested experimentally.

Author Contributions: Conceptualization, M.B. and P.V.; methodology, M.B. and P.V. software, M.B.; validation, M.B. and P.V.; formal analysis, M.B. and P.V.; investigation, M.B. and P.V.; resources, M.B. and P.V.; data curation, M.B.; writing—original draft preparation, M.B.; writing—review and editing, P.V.; visualization, M.B. All authors have read and agreed to the published version of the manuscript.

Funding: This research received no external funding.

Institutional Review Board Statement: Not applicable.

Informed Consent Statement: Not applicable.

Conflicts of Interest: The authors declare no conflict of interest.

References

1. Stockman, M.I. The spaser as a nanoscale quantum generator and ultrafast amplifier. *J. Opt.* **2010**, *12*, 024004. [CrossRef]
2. Ozbay, E. Plasmonics: Merging Photonics and Electronics at Nanoscale Dimensions. *Science* **2006**, *13*, 189–193. [CrossRef]
3. Brongersma, M.L.; Shalaev, V.M. The Case for Plasmonics. *Science* **2010**, *328*, 440–441. [CrossRef]
4. Gramotnev, D.K.; Bozhevolnyi, S.I. Plasmonics beyond the diffraction limit. *Nat. Photonics* **2010**, *4*, 83–91. [CrossRef]
5. Pacifici, D.; Lezec, H.J.; Atwater, H.A. All-optical modulation by plasmonic excitation of CdSe quantum dots. *Nat. Photonics* **2007**, *1*, 402–406. [CrossRef]
6. Boltasseva, A.; Atwater, H.A. Low-Loss Plasmonic Metamaterials. *Science* **2011**, *33*, 290–291. [CrossRef]
7. Tang, L.; Kocabas, S.E.; Latif, S.; Okyay, A.K.; Ly-Gagnon, D.; Saraswat, K.C.; Miller, D.A.B. Nanometre-scale germanium photodetector enhanced by a near-infrared dipole antenna. *Nat. Photonics* **2008**, *2*, 226–229. [CrossRef]
8. Maier, S.A.; Brongersma, M.L.; Kik, P.G.; Meltzer, S.; Requicha, A.A.G.; Atwater, H.A. Plasmonics—A route to nanoscale optical devices. *Adv. Mater.* **2001**, *13*, 1501. [CrossRef]
9. Wachter, S.; Polyushkin, D.K.; Bethge, O.; Mueller, T. A microprocessor based on a two-dimensional semiconductor. *Nat. Commun.* **2017**, *8*, 14948. [CrossRef] [PubMed]
10. H. A. Atwater, A. Polman Plasmonics for improved photovoltaic devices. *Nat. Mater.* **2010**, *9*, 205–213. [CrossRef] [PubMed]
11. Polman, A. Plasmonics Applied. *Science* **2008**, *322*, 868–869. [CrossRef]

12. Chen, J.; Badioli, M.; Alonso-Gonzalez, P.; Thongrattanasiri, S.; Huth, F.; Osmond, J.; Spasenovic, M.; Centeno, A.; Pesquera, A.; Godignon, P.; et al. Optical nano-imaging of gate-tunable graphene plasmons. *Nature* **2012**, *487*, 77–81. [CrossRef] [PubMed]
13. Fei, Z.; Rodin, A.S.; Andreev, G.O.; Bao, W.; McLeod, A.S.; Wagner, M.; Zhang, L.M.; Zhao, Z.; Thiemens, M.; Dominguez, G.; et al. Gate-tuning of graphene plasmons revealed by infrared nano-imaging. *Nature* **2012**, *487*, 82–85. [CrossRef]
14. Visser, T.D. Surface plasmons at work? *Nat. Phys.* **2006**, *2*, 509–510. [CrossRef]
15. Bahrami, M.; Vasilopoulos, P. Exchange, correlation, and scattering effects on surface plasmons in arm-chair graphene nanoribbons. *Opt. Express* **2017**, *25*, 16840–16853. [CrossRef] [PubMed]
16. Bozhevolnyi, S.I.; Khurgin, J.B. The case for quantum plasmonics. *Nat. Photonics* **2017**, *11*, 398–400. [CrossRef]
17. Yang, Y.; Kelley, K.; Sachet, E.; Campione, S.; Luk, T.S.; Maria, J.; Brener, M.L.B.S.I. Femtosecond optical polarization switching using a cadmium oxide-based perfect absorber. *Nat. Photonics* **2017**, *11*, 390–395. [CrossRef]
18. Hirsch, L.R.; Stafford, R.J.; Bankson, J.A.; Sershen, S.R.; Rivera, B.; Price, R.E.; Hazle, J.D.; Halas, N.J.; West, J.L. Nanoshell-mediated near-infrared thermal therapy of tumors under magnetic resonance guidance. *Proc. Natl Acad. Sci. USA* **2003**, *100*, 13549. [CrossRef]
19. Nagatani, N.; Tanaka, R.; Yuhi, T.; Endo, T.; Kerman, K.; Takamura, Y.; Tamiya, E. Gold nanoparticle-based novel enhancement method for the development of highly sensitive immunochromatographic test strips. *Sci. Technol. Adv. Mater.* **2006**, *7*, 270. [CrossRef]
20. Bergman, D.J.; Stockman, M.I. Surface Plasmon Amplification by Stimulated Emission of Radiation: Quantum Generation of Coherent Surface Plasmons in Nanosystems. *Phys. Rev. Lett.* **2003**, *90*, 027402. [CrossRef]
21. Anker, J.N.; Hall, W.P.; Lyandres, O.; Shah, N.C.; Zhao, J.; Van Duyne, R.P. Biosensing with plasmonic nanosensors. *Nat. Mater.* **2008**, *7*, 442–4532. [CrossRef]
22. Okamoto, K.; Niki, I.; Shvartser, A.; Narukawa, Y.; Mukai, T.; Scherer, A. Surface-plasmon-enhanced light emitters based on InGaN quantum wells. *Nat. Mater.* **2004**, *3*, 601–605. [CrossRef]
23. Sundararaman, R.; Narang, P.; Jermyn, A.S.; Goddard, W.A.; Atwater, H.A. Theoretical predictions for hot-carrier generation from surface plasmon decay. *Nat. Commun.* **2014**, *5*, 5788. [CrossRef] [PubMed]
24. Takahara, J.; Yamagishi, S.U.; Taki, H.; Morimoto, A.; Kobayashi, T. Guiding of a one-dimensional optical beam with nanometer diameter. *Opt. Lett.* **1997**, *22*, 475. [CrossRef]
25. Challener, W.A.; Peng, C.; Itagi, A.V.; Karns, D.; Peng, W.; Peng, Y.; Yang, X.; Zhu, X.; Gokemeijer, N.J.; Hsia, Y.T.; et al. Heat-assisted magnetic recording by a near-field transducer with efficient optical energy transfer. *Nat. Photonics* **2009**, *3*, 220–224. [CrossRef]
26. Cao, L.; Barsic, D.N.; Guichard, A.R.; Brongersma, M.L. Plasmon-Assisted Local Temperature Control to Pattern Individual Semiconductor Nanowires and Carbon Nanotubes. *Nano Lett.* **2007**, *7*, 3523–3527. [CrossRef] [PubMed]
27. Maier, S.A. *Plasmonics: Fundamentals and Applications*; Springer: New York, NY, USA, 2007.
28. Mikhailov, S.A.; Ziegler, K. New Electromagnetic Mode in Graphene. *PRL* **2007**, *99*, 016803. [CrossRef]
29. Giuliani, G.F.; Vignale, G. *Quantum Theory of the Electron Liquid*; Cambridge University: Cambridge, UK, 2005.
30. Jablan, M.; Buljan, H.; Soljacic, M. Plasmonics in graphene at infrared frequencies. *PRB* **2009**, *80*, 245435. [CrossRef]
31. Bahrami, M. Many-Body Effects in Novel Nanostructures: Optical and Transport Properties. Ph.D. Thesis, Concordia University, Montreal, OC, Canada, 2018.
32. Wunsch, B.; Stauber, T.; Sols, F.; Guinea, F. Dynamical polarization of graphene at finite doping. *New J. Phys.* **2006**, *8*, 318. [CrossRef]
33. Charbonneau, M.; Vliet, K.M.V.; Vasilopoulos, P. Linear response theory revisited III: One-body response formulas and generalized Boltzmann equations. *J. Math. Phys.* **1982**, *23*, 2. [CrossRef]
34. Van Vliet, C.M. *Equilibrium and Non-Equilibrium Statistical Mechanics*; World Scientific Press: Singapore, 2008.
35. Manzoni, M.T.; Silveiro, I.; de Abajo, F.J.G.; Chang, D.E. Second-order quantum nonlinear optical processes in single graphene nanostructures and arrays. *New J. Phys.* **2015**, *17*, 083031. [CrossRef]
36. Abajo, F.J.G. Graphene Plasmonics: Challenges and Opportunities. *ACS Photonics* **2014**, *1*, 135–152. [CrossRef]
37. Bosman, M.; Ye, E.; Tan, S.F.; Nijhuis, C.A.; Yang, J.K.W.; Marty, R.; Mlayah, A.; Arbouet, A.; Girard, C.; Han, M. Surface Plasmon Damping Quantified with an Electron Nanoprobe. *Sci. Rep.* **2013**, *3*, 1312. [CrossRef] [PubMed]